

Stability, electronic structure, and optical properties of lead-free perovskite monolayer Cs3B2X9 (B=Sb, Bi; X=Cl, Br, I) and bilayer vertical heterostructure Cs3B2X9/Cs3B2'X9 (B,B'=Sb, Bi; X=Cl, Br, I)

Yaowen Long(龙耀文), Hong Zhang(张红), and Xinlu Cheng(程新路)
Citation: Chin. Phys. B, 2022, 31 (**2**): 027102. DOI: 10.1088/1674-1056/ac2e5f
Journal homepage: http://cpb.iphy.ac.cn; http://iopscience.iop.org/cpb

What follows is a list of articles you may be interested in

Passivation and dissociation of P_b-type defects at a-SiO_2/Si interface

Xue-Hua Liu(刘雪华), Wei-Feng Xie(谢伟锋), Yang Liu(刘杨), and Xu Zuo(左旭)
Chin. Phys. B, 2021, 30 (**9**): 097101. DOI: 10.1088/1674-1056/ac0e20

Non-Hermitian Kitaev chain with complex periodic and quasiperiodic potentials

Xiang-Ping Jiang(蒋相平), Yi Qiao(乔艺), and Junpeng Cao(曹俊鹏)
Chin. Phys. B, 2021, 30 (**7**): 077101. DOI: 10.1088/1674-1056/abfa08

Tuning transport coefficients of monolayer $MoSi_2N_4$ with biaxial strain

Xiao-Shu Guo(郭小姝) and San-Dong Guo(郭三栋)
Chin. Phys. B, 2021, 30 (**6**): 067102. DOI: 10.1088/1674-1056/abdb22

Investigation of electronic, elastic, and optical properties of topological electride Ca_3Pb via first-principles calculations

Chang Sun(孙畅), Xin-Yu Cao(曹新宇), Xi-Hui Wang(王西惠), Xiao-Le Qiu(邱潇乐), Zheng-Hui Fang(方铮辉), Yu-Jie Yuan(袁宇杰), Kai Liu(刘凯), and Xiao Zhang(张晓)
Chin. Phys. B, 2021, 30 (**5**): 057104. DOI: 10.1088/1674-1056/abec38

Electronic structure and optical properties of Al and Mg co-doped GaN

Ji Yan-Jun, Du Yu-Jie, Wang Mei-Shan
Chin. Phys. B, 2013, 22 (**11**): 117103. DOI: 10.1088/1674-1056/22/11/117103

Stability, electronic structure, and optical properties of lead-free perovskite monolayer $Cs_3B_2X_9$ (B = Sb, Bi; X = Cl, Br, I) and bilayer vertical heterostructure $Cs_3B_2X_9/Cs_3B'_2X_9$ (B,B' = Sb, Bi; X = Cl, Br, I)

Yaowen Long(龙耀文)[1,2], Hong Zhang(张红)[1,2,†], and Xinlu Cheng(程新路)[3]

[1] *College of Physics, Sichuan University, Chengdu* 610065, *China*
[2] *Key Laboratory of High Energy Density Physics and Technology (Ministry of Education), Sichuan University, Chengdu* 610065, *China*
[3] *Institute of Atomic and Molecular Physics, Sichuan University, Chengdu* 610065, *China*

(Received 17 August 2021; revised manuscript received 18 September 2021; accepted manuscript online 11 October 2021)

The lead-free perovskites $Cs_3B_2X_9$ (B = Sb, Bi; X = Cl, Br, I) as the popular photoelectric materials have excellent optical properties with lower toxicity. In this study, we systematically investigate the stable monolayer $Cs_3B_2X_9$ and bilayer vertical heterostructure $Cs_3B_2X_9/Cs_3B'_2X_9$ (B, B' = Sb, Bi; X = Cl, Br, I) via first-principles simulations. By exploring the electrical structures and band edge positions, we find the band gap reduction and the band type transition in the heterostructure $Cs_3B_2X_9/Cs_3B'_2X_9$ due to the charge transfer between layers. Furthermore, the results of optical properties reveal light absorption from the visible light to UV region, especially monolayer $Cs_3Sb_2I_9$ and heterostructure $Cs_3Sb_2I_9/Cs_3Bi_2I_9$, which have absorption peaks in the visible light region, leading to the possibility of photocatalytic water splitting. These results provide insights for more two-dimensional semiconductors applied in the optoelectronic and photocatalytic fields.

Keywords: first principles simulations, lead-free perovskite, monolayer $Cs_3B_2X_9$, vertical heterostructure $Cs_3B_2X_9/Cs_3B'_2X_9$, photoelectric materials

PACS: 71.20.–b, 71.15.Mb, 73.40.Lq, 31.15.A– **DOI:** 10.1088/1674-1056/ac2e5f

1. Introduction

In recent years, lead-free perovskites have attracted widespread attention and interest due to their non-toxic and unique optoelectronic properties.[1–3] A large number of studies on 3D perovskites, such as Bi-based cesium bismuth halides, Sb-based cesium antimony halides, double perovskite semiconductor $Cs_2Sn_{1-x}Te_xI_6$ and $Cs_2Ag_xNa_{1-x}InCl_6$ powders,[1,4–6] have shown that they have well performance in photocatalytic water splitting, light-emitting diodes and solar cell applications.

Among those lead-free perovskites, $Cs_3B_2X_9$ (B = Sb, Bi; X = Cl, Br, I) compositions have been investigated as a promising material group due to their good properties. In 2019, Yousra *et al.*[7] reported that $Cs_3B_2X_9$ could be synthesized through dry mechanochemistry and showed white-light emission at room temperature through experiment. Moreover, first-principle studies of electronic and optical properties of $Cs_3Sb_2X_9$ revealed that the absorption red shifts from Cl to I as the band gap decreases.[4] Although 3D perovskites have experienced unprecedent rapid development in those years, their stability under the light and heat is still an important reason hindering their commercial applications.[8,9] Therefore, the corresponding two-dimensional perovskites have attracted more and more attention due to their excellent 2D quantum confinement effects.[10–13] The 2D halide perovskites are basically divided into two groups: inorganic layer and organic cation diversity. Lanzetta *et al.*[14] investigated the 2D organic tin halide perovskites $(PEA)_2SnI_XBr_{4-x}$ with tunable optical properties in the visible spectrum by changing the I/Br ratio. Pan *et al.*[15] investigated the layer-number-dependent electrical and optical properties of the all-inorganic 2D RP perovskite $Cs_2PbI_2Cl_2$ and emphasized that the excition-binding energy increases with the decreasing number of layers, which provides theoretical support to applications of 2D perovskites in photoelectric devices. In addition, we can also adjust the electrical and optical properties of perovskites by the composition, pressure or construction of heterostructures.[16–19] As mentioned above, lead-free perovskites based on Cs cation have been extensively studied, and the successfully synthesized 2D ultrathin few-layer (2–4 layers) $Cs_3Bi_2I_9$ provides a direction for the theoretical calculation.[20] In previous studies, there have not been systematic theoretical calculations for the two-dimensional monolayer $Cs_3B_2X_9$ perovskite, especially for stability of these substances.

In this article, we perform a systematic study of electronic, stability and optical properties of all-inorganic 2D

†Corresponding author. E-mail: hongzhang@scu.edu.cn

© 2022 Chinese Physical Society and IOP Publishing Ltd

monolayer $Cs_3B_2X_9$ via first-principles density functional theory. In Section 2, we give a comprehensive description of the calculation details. In Section 3, firstly we check the stability of monolayer $Cs_3B_2X_9$ (B = Sb, Bi; X = Cl, Br, I), secondly we study their electronic structures, thirdly we analyze the feasibility of their photocatalytic water splitting through the work function and optical absorption, fourthly stability, electronic and optical properties of the heterostructure $Cs_3B_2X_9/Cs_3B'_2X_9$ (B,B' = Sb, Bi; X = Cl, Br, I) are discussed. Finally, in Section 4 we summarize all the results.

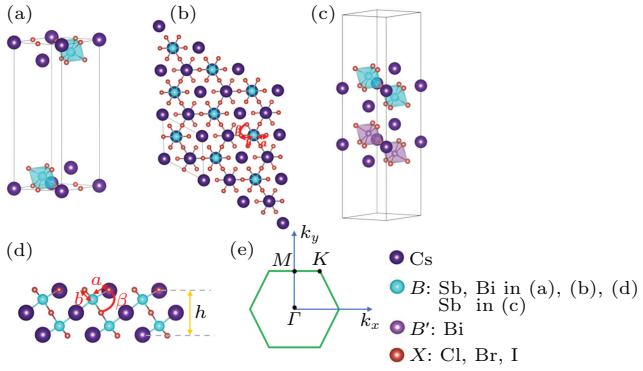


Fig. 1. (a), (b) and (d) Stereogram, top view, side view of the 2D monolayer $Cs_3B_2X_9$, respectively, tagged with structure parameters. (c) The stereogram of heterostructure $Cs_3B_2X_9/Cs_3B'_2X_9$ (B,B' = Sb, Bi; X = Cl, Br, I). (e) The schematic diagram represents the Brillouin zone of the 2D monolayer $Cs_3B_2X_9$ with high symmetric points Γ, M, K.

2. Computational details

All the calculations in this paper are based on first-principles density functional theory. Using the CASTEP[21] package for structural relaxation and phonon dispersions, we take different plane-wave cutoff energies from 400 eV to 750 eV to improve the computational efficiency for different systems and select the norm-conserving pseudopotentials. We utilize the approximation (GGA) represented by the Perdew–Burke–Ernzerhof (PBE) functional[22] to compute the phonon dispersions of the structure. The geometry optimization is finished when max ionic tolerance is lower than 0.03 eV/Å and the energy tolerances are less than 10^{-4} per atom. We sample $2\times2\times1$ grid of k-point by Monkhorst–Pack scheme in Brillouin zone. The phonon dispersions are calculated by the linear response method.[23]

In order to further study more about these materials, we make some calculations about monolayer $Cs_3B_2X_9$ band structures using the Heyd–Scuseria–Ernzerhof (HSE06) hybrid functional since it is able to accurately calculate the band gap.[24] We also use it to get their work function and optical properties. Furthermore, we consider the effect of the van der Waals force using the DFT-D3 correction method of Grimme to compute the heterostructure $Cs_3B_2X_9/Cs_3B'_2X_9$ (B,B' = Sb, Bi; X = Cl, Br, I).[25] The k-point we make is $6\times6\times1$ grid of k-point by Monkhorst–Pack scheme in Brillouin zone and the energy (both total energy and band structure energy) change between two steps is smaller than 10^{-8} eV. The plane-wave cutoff energy is set to 400 eV. All the calculations for this section are carried out using the Vienna *ab initio* simulation package (VASP).[26]

3. Results and discussion

3.1. Stability of monolayer $Cs_3B_2X_9$ (B = Sb, Bi; X = Cl, Br, I)

Here we give a brief description of this structure. The 2D monolayer $Cs_3B_2X_9$ is a structure consisting of dioctahedral $B_2X_9^{3-}$ dimer-like units with corner-sharing connectivity surrounded by cesium cations (Fig. 1(a)). The vacuum layer between the upper and lower layers in the z-axis direction is about 20 Å. The space-group symmetries of the monolayers $Cs_3B_2X_9$ are all $P\bar{3}M1$ and some of them are different from their 3D structures. For instance, the three-dimensional crystal structure of $Cs_3Bi_2I_9$ is $P63/MMC$.[27]

Table 1. The results for optimized geometries and cohesive energies of monolayer $Cs_3Bi_2X_9$ obtained using DFT with PBE.

Structure	Cohesive energy (eV/atom)	Lattice constant (Å)	Layer height h (Å)	Bond length $a(b)$ (Å)	Bond angle β (°)
$Cs_3Sb_2Cl_9$	–3.314	7.715	6.261	2.435(2.865)	90.988
$Cs_3Sb_2Br_9$	–2.964	7.935	6.556	2.600(2.961)	90.899
$Cs_3Sb_2I_9$	–2.602	8.569	7.076	2.835(3.189)	90.728
$Cs_3Bi_2Cl_9$	–3.344	7.704	6.252	2.541(2.866)	89.743
$Cs_3Bi_2Br_9$	–2.992	8.029	6.577	2.681(2.996)	89.871
$Cs_3Bi_2I_9$	–2.626	8.646	7.135	2.912(3.237)	89.973

After the full structural relaxations, we obtain some structural information which included lattice constants, bond length and bond angle of monolayer $Cs_3B_2X_9$ as shown in Figs. 1(a) and 1(d). The corresponding values are all listed in Table 1. To verify the stability of the monolayer $Cs_3B_2X_9$ structure, we perform calculations of the cohesive energy and calculations of the phonon dispersion. To calculate the cohesive energy E_{coh} of monolayer $Cs_3B_2X_9$, we use the standard formula

$$E_{coh} = \frac{E_{tot} - 3E_{atom}(Cs) - 2E_{atom}(B) - 9E_{atom}(X)}{14}, \quad (1)$$

where E_{tot} is the total energy of monolayer $Cs_3B_2X_9$, and E_{atom} is the energy of each free atom, which is obtained by performing an isolated atom in a vacuum layer with a lattice constant of 15 Å, avoiding the interaction between adjacent atoms. The cohesive energies listed in Table 1 are −3.314 eV ($Cs_3Sb_2Cl_9$), −2.964 eV ($Cs_3Sb_2Br_9$), −2.602 eV ($Cs_3Sb_2I_9$), −3.344 eV ($Cs_3Bi_2Cl_9$), −2.992 eV ($Cs_3Bi_2Br_9$), −2.626 eV ($Cs_3Bi_2I_9$). In the case of the same halogen atom, the absolute value of cohesive energy (see Table 1) of the monolayer $Cs_3Bi_2X_9$ is slightly higher than the monolayer $Cs_3Sb_2X_9$, illustrating better stability of monolayer $Cs_3Bi_2X_9$.

To further explore the stability of the monolayer perovskites $Cs_3B_2X_9$, we execute the phonon dispersion. The results (Fig. 2) show that the lead-free monolayer perovskites $Cs_3B_2X_9$ in the Brillouin zone along a high symmetry point path (Fig. 1(e)) have fully positive phonon dispersion. The minimum acoustic branch near the gamma point is linear, meeting the expected results for the long-wave approximation, which demonstrates the dynamical stability of these monolayer $Cs_3B_2X_9$ compounds.

Combined with the above detailed analyses of the cohesive energy and phonon dispersion, we can conclude theoretically that the monolayer $Cs_3B_2X_9$ (B = Sb, Bi; X = Cl, Br, I) can exist stably.

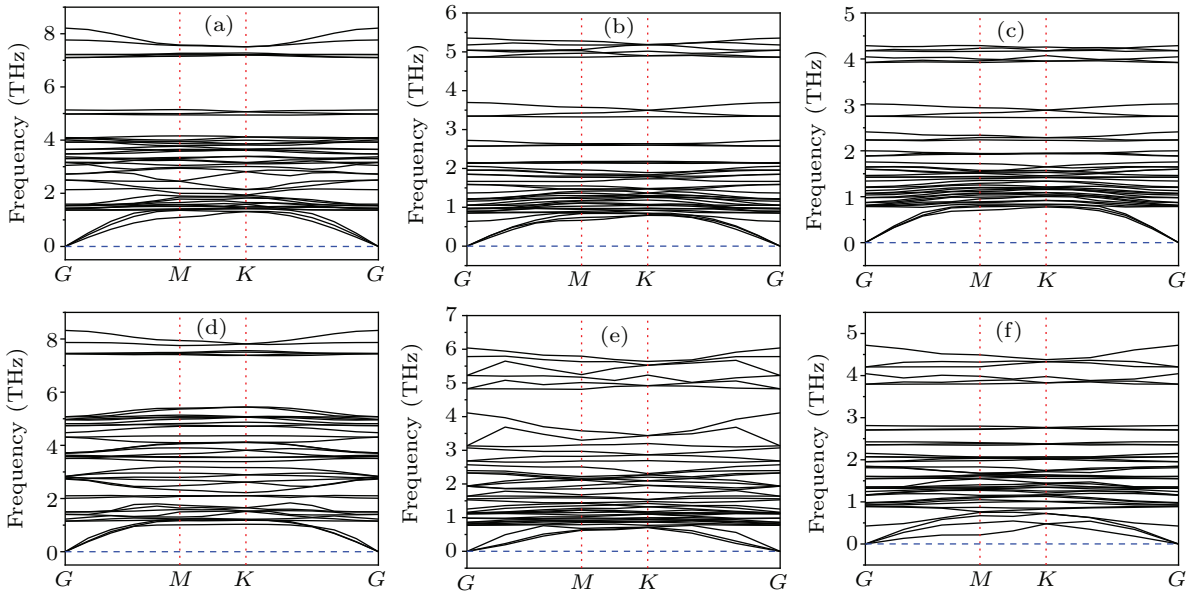


Fig. 2. (a)–(f) The phonon dispersion of $Cs_3Bi_2Cl_9$, $Cs_3Bi_2Br_9$, $Cs_3Bi_2I_9$, $Cs_3Sb_2Cl_9$, $Cs_3Sb_2Br_9$, $Cs_3Sb_2I_9$, respectively.

3.2. Band structures of monolayer $Cs_3B_2X_9$ (B = Sb, Bi; X = Cl, Br, I)

Before exploring the heterostructure $Cs_3B_2X_9/Cs_3B'_2X_9$ (B,B' = Sb, Bi; X = Cl, Br, I), the calculations of monolayer $Cs_3B_2X_9$ (B = Sb, Bi; X = Cl, Br, I) band structures are carried out using HSE06 hybrid functional (see Fig. 3). The bandgaps of monolayer cesium bismuth halides are 4.198 eV ($Cs_3Bi_2Cl_9$), 3.564 eV ($Cs_3Bi_2Br_9$), 2.874 eV ($Cs_3Bi_2I_9$), as shown in Figs. 3(a)–3(c), and the bandgaps of monolayer cesium antimony halides are 3.503 eV ($Cs_3Sb_2Cl_9$), 2.981 eV ($Cs_3Sb_2Br_9$), 2.476 eV ($Cs_3Sb_2I_9$), as shown in Figs. 3(d)–3(f). Compared with the 3D crystal structure $Cs_3B_2X_9$, the band gap of the monolayer structure is higher due to its 2D electronic dimensionality (quantum confinement effects), which can cause lower VB maximums (VBMs) and higher CB minimums (CBMs).[4,28] One can see that the $Cs_3Bi_2X_9$ type monolayer perovskites are all indirect bands with the VBMs occurring along the G–M direction and CBMs located at G point, as shown in Figs. 3(a)–3(c). For $Cs_3Sb_2X_9$-type monolayer perovskites, the similar pattern occurs except monolayer $Cs_3Sb_2Cl_9$ which VBM is located at G, and CBM appears between G and M. Comparing monolayer cesium bismuth halides and cesium antimony halides, we find about 0.5 eV more band gaps in V-group element bismuth. Therefore, the wide bandgap of $Cs_3Bi_2X_9$ can apply to high-power electronic devices and UV light devices. Furthermore, the band gap decreases as the weight of the halogen atom increases in both $Cs_3Sb_2X_9$ and $Cs_3Bi_2X_9$, especially for $Cs_3Sb_2I_9$ with only 2.476 eV. This means that 2D monolayer $Cs_3Sb_2X_9$ has potential applications in visible light devices.

Kim *et al.*[16] reported that band gap increases as the B–X distance decreases in the crystal structure of $Cs_3B_2X_9$, and the same features of monolayer structure show up (see Table 8). They also reported that the band gap increases as the electronegativity difference between the B site metal and X site halide increases, which is consistent with our present result (Fig. 3). However, the bond angle β (Figs. 1(b) and 1(d))

between two asymmetric atoms B relative to central atom X shows an opposite trend in $Cs_3Sb_2X_9$ and $Cs_3Bi_2X_9$. With the increase of band gap, the bond angle β of $Cs_3Sb_2X_9$ increases and the bond angle β of $Cs_3Bi_2X_9$ decreases.

To understand the contribution of each element and the electronic states of its different orbitals to the band, we perform calculations of total densities of states (TDOS) and partial densities of states (PDOS) of the monolayer $Cs_3B_2X_9$ near the Fermi level. Due to few contributions of d-orbital of all elements to the electronic states near the Fermi level, we omit it when drawing, and the results are shown in Fig. 4. The more details of DOS are placed in Appendix A.

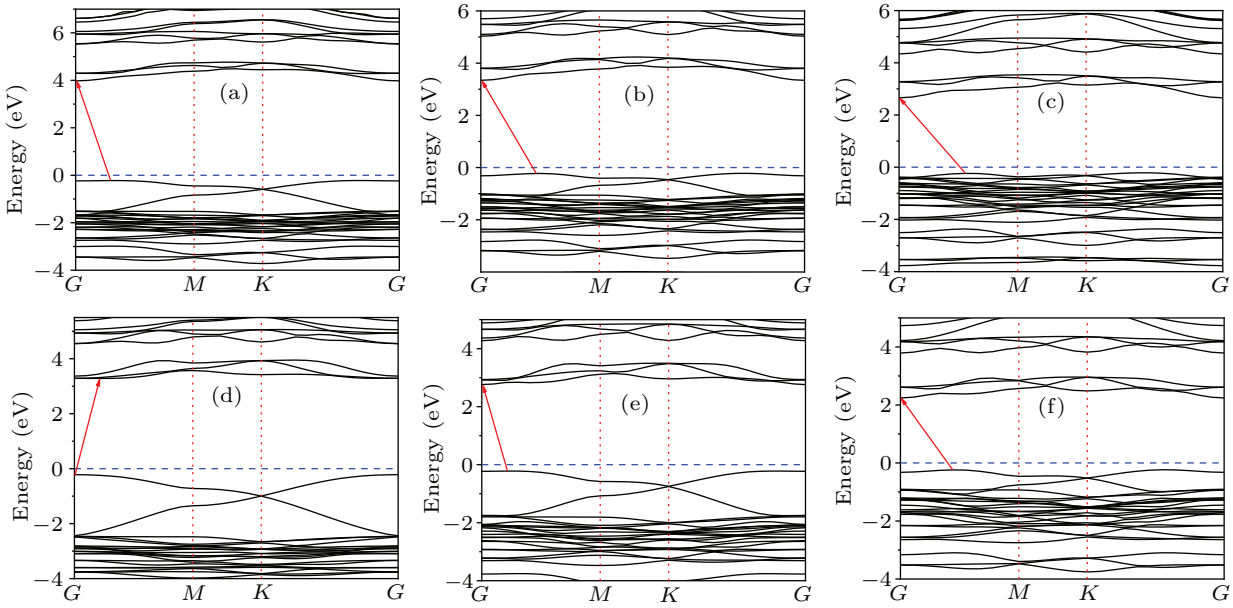


Fig. 3. (a)–(c) Band structures of monolayer $Cs_3Bi_2Cl_9$, $Cs_3Bi_2Br_9$, $Cs_3Bi_2I_9$, respectively. (d)–(f) Band structures of monolayer $Cs_3Sb_2Cl_9$, $Cs_3Sb_2Br_9$, $Cs_3Sb_2I_9$. The blue dashed line represents the Fermi level set to zero. The location of the band gap is indicated by the red arrows.

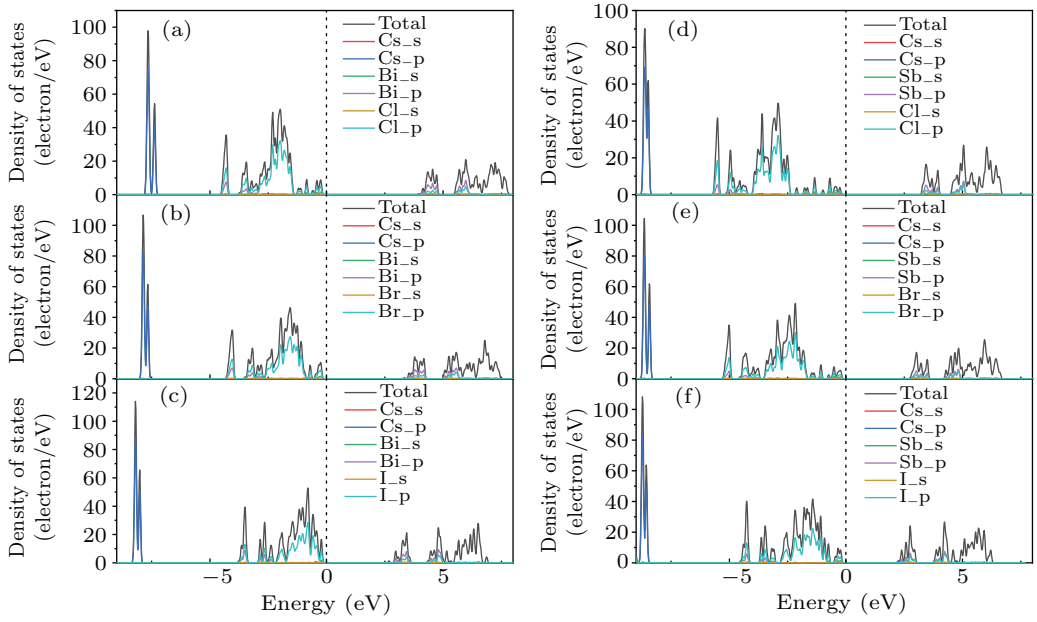


Fig. 4. (a)–(c) TDOS and PDOS of the monolayer $Cs_3Bi_2X_9$ (X = Cl, Br, I), respectively. (d)–(f) TDOS and PDOS of the monolayer $Cs_3Sb_2X_9$ (X = Cl, Br, I). The black dashed line represents the Fermi energy level set to zero.

It is observed from the PDOS of all six types of monolayer $Cs_3B_2X_9$ that the state near the Fermi level has contributions from the s orbital of B (Sb, Bi), the p orbital of X (Cl, Br, I) and B (Sb, Bi). We can find that the states closest to the CBM of all monolayer $Cs_3B_2X_9$ have contributions from the p orbitals of B (Sb, Bi) and X (Cl, Br, I). This suggests the existence of anti-bonding states due to the strong interaction between the p orbitals of B and X. In the case of the state closest to the VBM, the contributions from the s orbitals of B (Sb, Bi) and the p orbitals of X (Cl, Br, I) imply a typical s–p interaction of the orbital hybridization of B (Sb, Bi) and X (Cl, Br, I) atoms. In addition, the lower energy region of the valence

band is occupied by electrons in the p orbitals, indicating that the existence of bonding states due to the interaction between the B (Sb, Bi) and the X (Cl, Br, I) atoms. In general, with the increase of atomic number of X (Cl, Br, I), the density of states near the Fermi level also increases, which provides convenience for the excitation of photogenerated carriers, suggesting its potential applications in optoelectronic devices.

3.3. Monolayer $Cs_3B_2X_9$ (B = Sb, Bi; X = Cl, Br, I) for water splitting

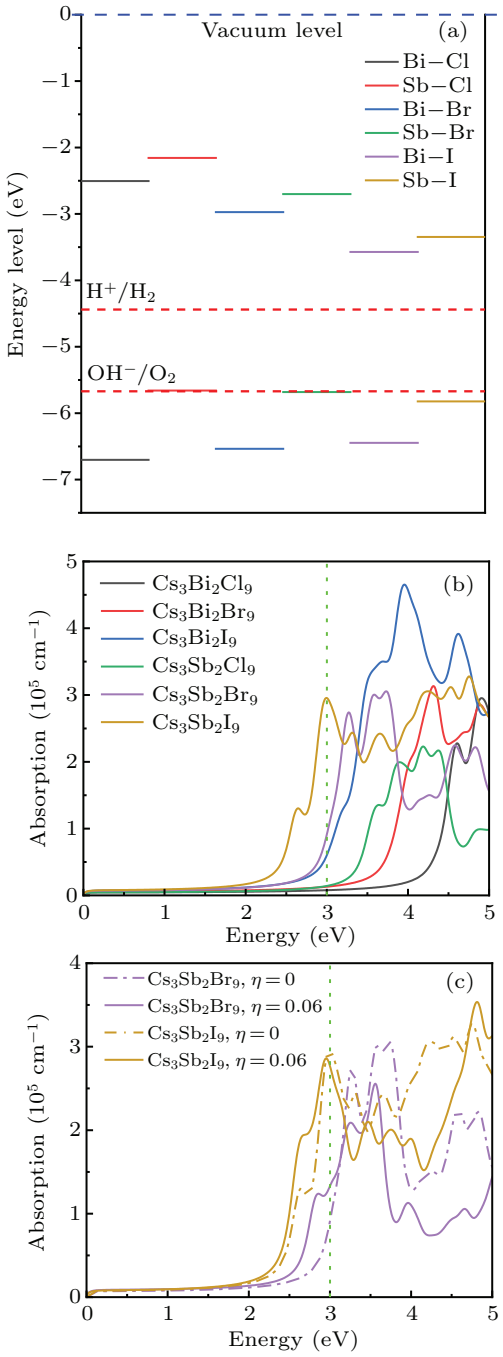


Fig. 5. (a) Band edge position of monolayer $Cs_3B_2X_9$ (B = Sb, Bi; X = Cl, Br, I) relative to the vacuum level (blue dashed line) calculated with HSE06 functional. The redox potential is marked with red dotted lines, and the legends B–X (B = Sb, Bi; X = Cl, Br, I) represent monolayer $Cs_3B_2X_9$ (B = Sb, Bi; X = Cl, Br, I). (b) The absorption spectra of monolayer $Cs_3B_2X_9$. (c) The absorption spectra of monolayer $Cs_3Sb_2Br_9$ and $Cs_3Sb_2I_9$ before and after applying the mechanical biaxial strain.

As we all know, a good photocatalyst material needs a suitable band alignment. We have calculated the values of CBM and VBM via the hybridized functional HSE06 and determined the work function of the monolayer $Cs_3B_2X_9$ by calculating the vacuum level (see Fig. 5).

In order to become an excellent candidate for the semiconductor material, the band edges must straddle the water redox potentials, which means that the VBM should be above the reduction potential ($V_{H^+/H_2} = -4.44$ eV) and the CBM should be below the oxidation potential ($V_{OH^-/O_2} = -5.67$ eV). As shown in Fig. 5(a), almost all monolayer perovskites $Cs_3B_2X_9$ meet the requirement of the band alignment. However, the band gap of photocatalyst driven by visible light should be less than 3.0 eV ($\lambda > 415$ nm).[29] Herein, the monolayer $Cs_3Sb_2Br_9$, $Cs_3Bi_2I_9$ and $Cs_3Sb_2I_9$, corresponding to the green, purple and brown lines in Fig. 5(a), can be used as potential materials for visible light photocatalytic equipment.

In addition, we can see from the light absorption spectra (see Fig. 5(b)) that there are light absorptions in the visible region of $Cs_3Sb_2I_9$ and near-UV regions of $Cs_3Sb_2Br_9$, $Cs_3Bi_2I_9$ monolayer lead-free perovskite, especially in $Cs_3Sb_2I_9$, which shows an absorption peak in visible light region. Geng *et al.*[17] have reported that the absorption edge of nanomaterial $Cs_3Bi_2Br_9$ exhibits a redshift with the increase of pressure, indicating a possible way to obtain the visible light absorption for monolayer $Cs_3Sb_2Br_9$, $Cs_3Bi_2I_9$. Furthermore, compared the changes in the light absorption coefficient of monolayer $Cs_3Sb_2Br_9$ and $Cs_3Sb_2I_9$ before and after applying the mechanical biaxial strain, it is seen that the red shifts occur with a $\eta = 6\%$ compression (see Fig. 5(c)). This implies that the visible light absorption of monolayer $Cs_3B_2X_9$ can be achieved by applying an appropriate pressure.

3.4. Stability, band structure and optical properties for bilayer $Cs_3B_2X_9/Cs_3B'_2X_9$ (B, B' = Sb, Bi; X = Cl, Br, I) heterostructure

For the photocatalytic water splitting and photodetection, maintaining a long electron-hole recombination time is helpful for better detection and catalytic chemical reaction applications. The indirect band gap of monolayer $Cs_3B_2X_9$ must use the recombination center when conducting band electrons are recombined with valence band holes. Although the absorption efficiency is reduced in this process, the recombination time of electron-hole is prolonged ($\sim$ ns) in contrast to some direct band gap materials ($\sim$ ps).[30] In order to modulate the bandgap and obtain a longer carrier lifetime, two different two-dimensional monolayer semiconductors are usually connected into a vertical heterostructure (HS).[31] Here, we can more easily combine $Cs_3B'_2X_9$ (B' = Bi) and $Cs_3B_2X_9$ (B = Sb) to HS

due to their tiny mismatches of lattice constants, which are less than 1%.

We first calculate the binding energy of the heterojunction to investigate the structural stability. A standard formula of binding energy is given as follows:

$$E_{\text{bind}} = E_{\text{HS}} - E_{\text{layer}}(Cs_3B_2X_9) - E_{\text{layer}}(Cs_3B'_2X_9), \quad (2)$$

where E_{HS} is the total energy of HS $Cs_3B_2X_9/Cs_3B'_2X_9$ (B,B' = Sb, Bi; X = Cl, Br, I), and $E_{\text{layer}}(Cs_3B_2X_9)$, $E_{\text{layer}}(Cs_3B'_2X_9)$ are the energy of the ground state monolayer $Cs_3B_2X_9$ (B = Sb; X = Cl, Br, I) and the ground state monolayer $Cs_3B'_2X_9$ (B' = Bi; X = Cl, Br, I), respectively. The binding energies of HS (see Table 2) are −5.970 eV, −7.031 eV, −6.917 eV. Those are exothermic processes, indicating that the HS energy is reduced through the modulation of van der Waals forces.

Table 2. The parameters of HS $Cs_3B_2X_9/Cs_3B'_2X_9$ (B,B' = Sb, Bi; X = Cl, Br, I) after structure relaxation using the PBE exchange-correlation functional.

Structure	Lattice constant (Å)	Binding energy (eV)
$Cs_3Bi_2Cl_9/Cs_3Sb_2Cl_9$	7.710	–5.970
$Cs_3Bi_2Br_9/Cs_3Sb_2Br_9$	8.021	–7.031
$Cs_3Bi_2I_9/Cs_3Sb_2I_9$	8.607	–6.917

We next explore the band structures and density of states of the $Cs_3B_2X_9/Cs_3B'_2X_9$ (B,B' = Sb, Bi; X = Cl, Br, I), as shown in Fig. 6, with band gaps 3.133 eV (direct band), 2.659 eV (indirect band) and 2.143 eV (indirect band). Compared to the monolayer $Cs_3B_2X_9$, an obvious band gap decrease is found in the heterojunction, which implies an easier way for electron excitation from valence band to conduction band under the light. Moreover, the changing in band gap type of $Cs_3Sb_2Cl_9/Cs_3Bi_2Cl_9$ can be explained through the PDOS and band structure, as shown in Figs. 6(a), 6(d), 6(g). The states near the VBM are occupied by the $Cs_3Sb_2Cl_9$ layer and the states near the CBM are occupied by the $Cs_3Bi_2Cl_9$ layer, which means that the excitation of electrons is energetically favorable from the VBM of $Cs_3Sb_2Cl_9$ (G point in monolayer structure) to the CBM of $Cs_3Bi_2Cl_9$ (G point in monolayer structure).

From the performed PDOS and band structures in Fig. 6, it can be seen that all the three HS share the same trend that the VBM is dominated by the states from $Cs_3Sb_2X_9$ layer whereas the CBM is mainly provided by the states from $Cs_3Bi_2X_9$ layer. Furthermore, the valence band offset (VBO) and conduction band offset (CBO) between the $Cs_3Sb_2X_9$ and $Cs_3Bi_2X_9$ layers can be seen in Fig. 5(a), indicating the existence of the type Ⅱ band alignment. Therefore, the transmission of photo-generated holes from $Cs_3Bi_2X_9$ to $Cs_3Sb_2X_9$ can be achieved through VBO and the electrons can be transferred from $Cs_3Sb_2X_9$ to $Cs_3Bi_2X_9$ powered by CBO.

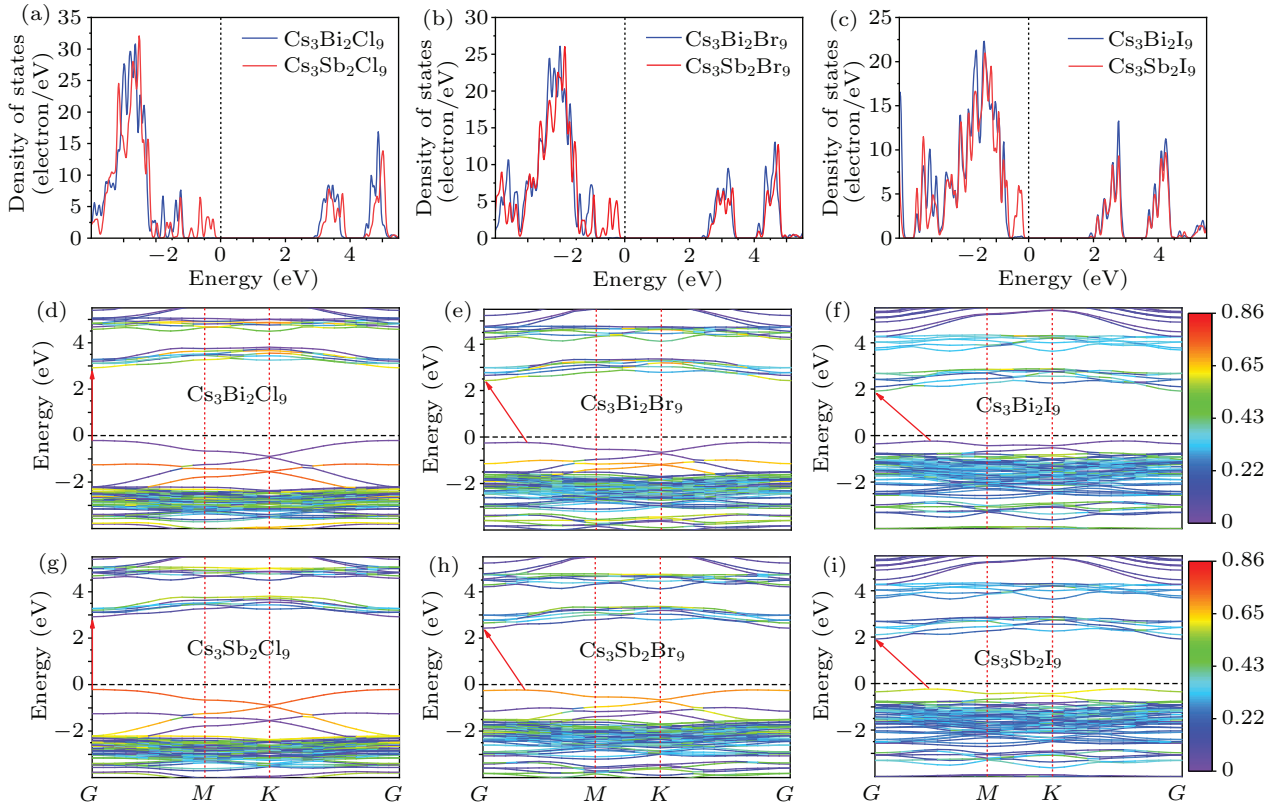


Fig. 6. (a)–(c) Projected density of states (PDOS) and (d)–(i) projected band structures (PBANDS) of heterostructures $Cs_3B_2X_9/Cs_3B'_2X_9$ (B,B' = Sb, Bi; X = Cl, Br, I), respectively.

With the increase of the halogen atomic number of HS, it is observed that the states near the Fermi level are increased and give a narrower band gap (see Fig. 6). Unlike the alloy-induced phase transition,[27] $Cs_3Sb_2I_9/Cs_3Bi_2I_9$ shows the most appropriate band gap for water splitting under the visible light, which is tuned by the charge transfer between layers, as shown in Fig. 7(a). The type Ⅱ band alignment caused by the interlayer electron excitation could adjust the electron transfer behavior as mentioned above to reduce the band gap. Photoinduced electron and hole transfers on different sides of the heterojunction promote charge-carrier separation to prevent rapid recombination of photogenerated carriers. Therefore, we explore the optical properties about heterostructure $Cs_3B_2X_9/Cs_3B'_2X_9$ (B,B' = Sb, Bi; X = Cl, Br, I).

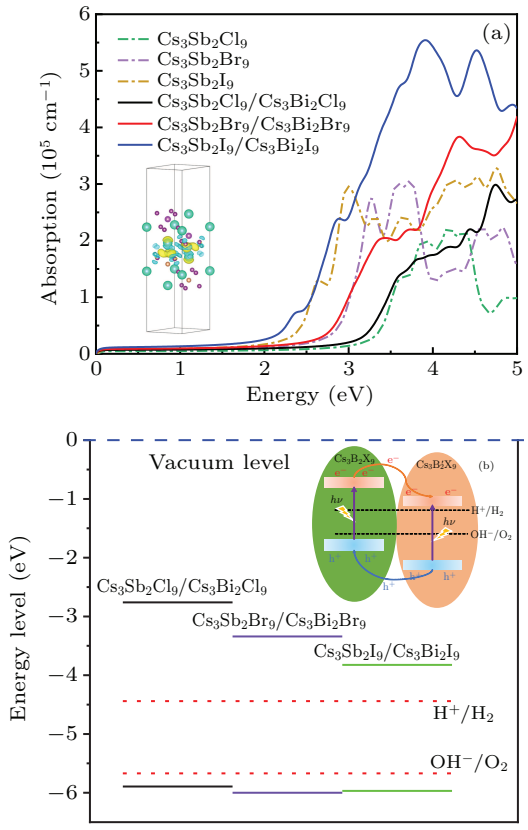


Fig. 7. (a) Absorption spectra of $Cs_3B_2X_9/Cs_3B'_2X_9$ and $Cs_3Sb_2X_9$, the differential charge density of heterostructure $Cs_3Sb_2I_9/Cs_3Bi_2I_9$ (see inset). (b) Band edge position of heterostructures $Cs_3B_2X_9/Cs_3B'_2X_9$ relative to the vacuum level (blue dashed line) calculated with the HSE06 functional, and the schematic of the band alignment (see inset).

The frequency-dependent dielectric function is calculated, and then the absorption coefficient as photon energy is evaluated. Compared with the monolayer structure, the heterostructures $Cs_3B_2X_9/Cs_3B'_2X_9$ show absorption redshifts in the visible region, see Fig. 7(a), which meet the reduction of band gap. The overall absorption of light is enhanced, while there are some small decreases in different photon energy ranges ($\sim$ 3 eV of $Cs_3Sb_2I_9/Cs_3Bi_2I_9$, $\sim$ 3.5 eV of $Cs_3Sb_2Br_9/Cs_3Bi_2Br_9$ and $\sim$ 4 eV of $Cs_3Sb_2Cl_9/Cs_3Bi_2Cl_9$). They all achieve significant light absorption in the near-UV regions (for 3 eV–5 eV). However, only the $Cs_3Sb_2I_9/Cs_3Bi_2I_9$ shows satisfactory visible light absorption. The difference of CBM could become the main reason to modify the light absorption, in the case of similar VBM, as shown in Fig. 7(b). In practical applications, substrates are often added to support and grow the materials. They could adjust the absorption coefficient via the internal distance between materials and the polar substrates.[32] Therefore, the selection of suitable substrate may provide an idea for further optimization of the absorption coefficient of heterojunction $Cs_3B_2X_9/Cs_3B'_2X_9$.

4. Conclusions

In summary, we have theoretically investigated the structural stability, electronic structure and optical properties of monolayer $Cs_3B_2X_9$ (B = Sb, Bi; X = Cl, Br, I) and heterostructure $Cs_3B_2X_9/Cs_3B'_2X_9$ (B,B' = Sb, Bi; X = Cl, Br, I) based on first-principles calculations. The stability of monolayer structures is verified through cohesive energy and phonon dispersion, and the stability of heterostructures is checked by binding energy. For monolayer structures, the indirect band gaps from $\sim$ 2.5 eV to $\sim$ 4.2 eV and band edge positions warrant good light absorption in the visible and near-UV region, which can be adjusted by appropriate pressure to achieve the redshift of light absorption. For the heterostructures $Cs_3B_2X_9/Cs_3B'_2X_9$, the band gaps from $\sim$ 2.1 eV to $\sim$ 3.1 eV reduction are observed due to the type Ⅱ band alignment, which shows different states occupied in different layers near the CBM and VBM. Moreover, the changing of band type from indirect to direct at Γ point is found in $Cs_3Sb_2Cl_9/Cs_3Bi_2Cl_9$ due to a particular way of charge transfer between layers. The $Cs_3Sb_2I_9/Cs_3Bi_2I_9$ shows satisfactory visible light absorption which is suitable for photocatalytic water splitting, while the other two show excellent absorption in near-UV region. The above results provide more options for photocatalytic applications of two-dimensional semiconductors.

Acknowledgements

This work was supported by the National Key R&D Program of China (Grant No. 2017YFA0303600), the National Natural Science Foundation of China (Grant No. 11974253), and the Science Specialty Program of Sichuan University (Grand No. 2020SCUNL210).

Appendix A

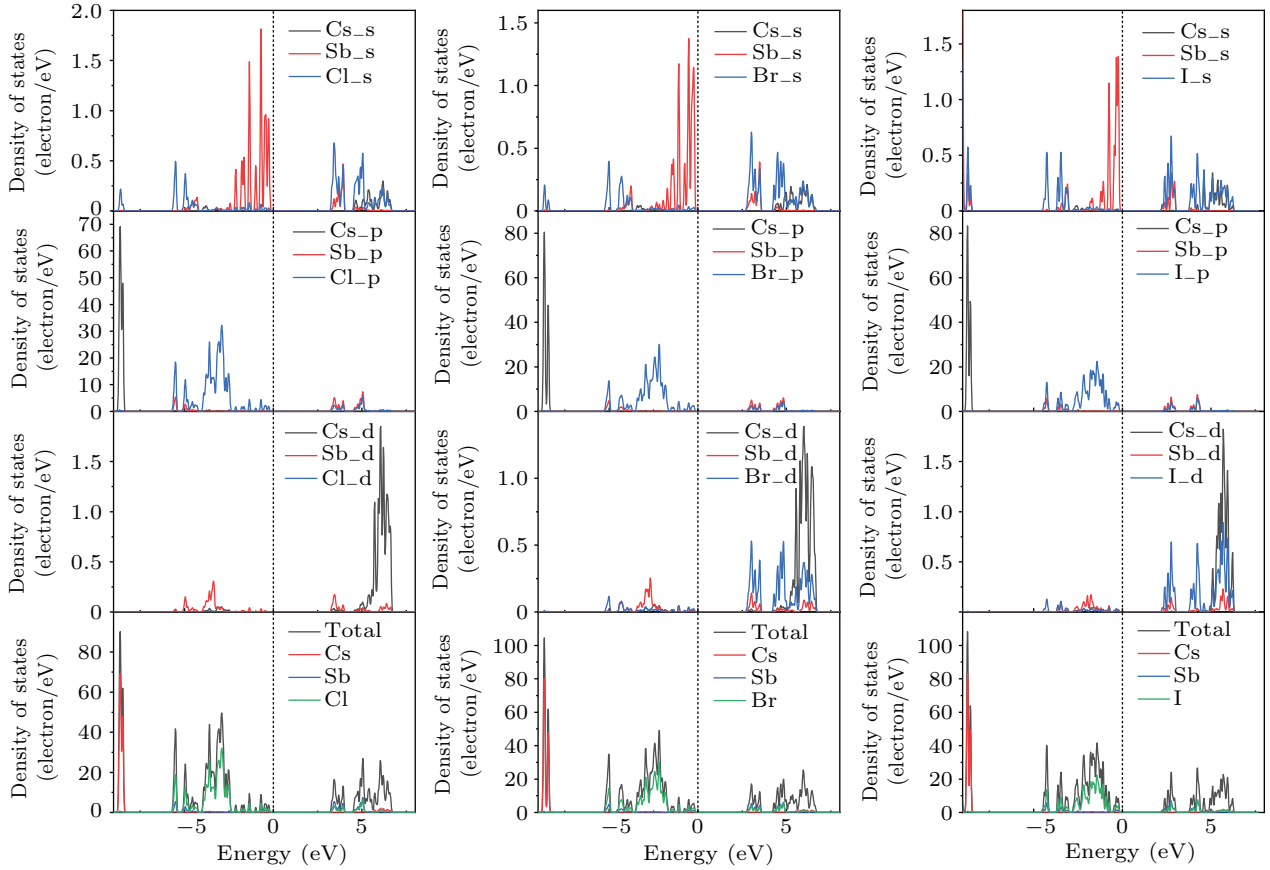


Fig. A1. The DOS of different orbitals and elements of monolayer $Cs_3Sb_2X_9$ (X = Cl, Br, I).

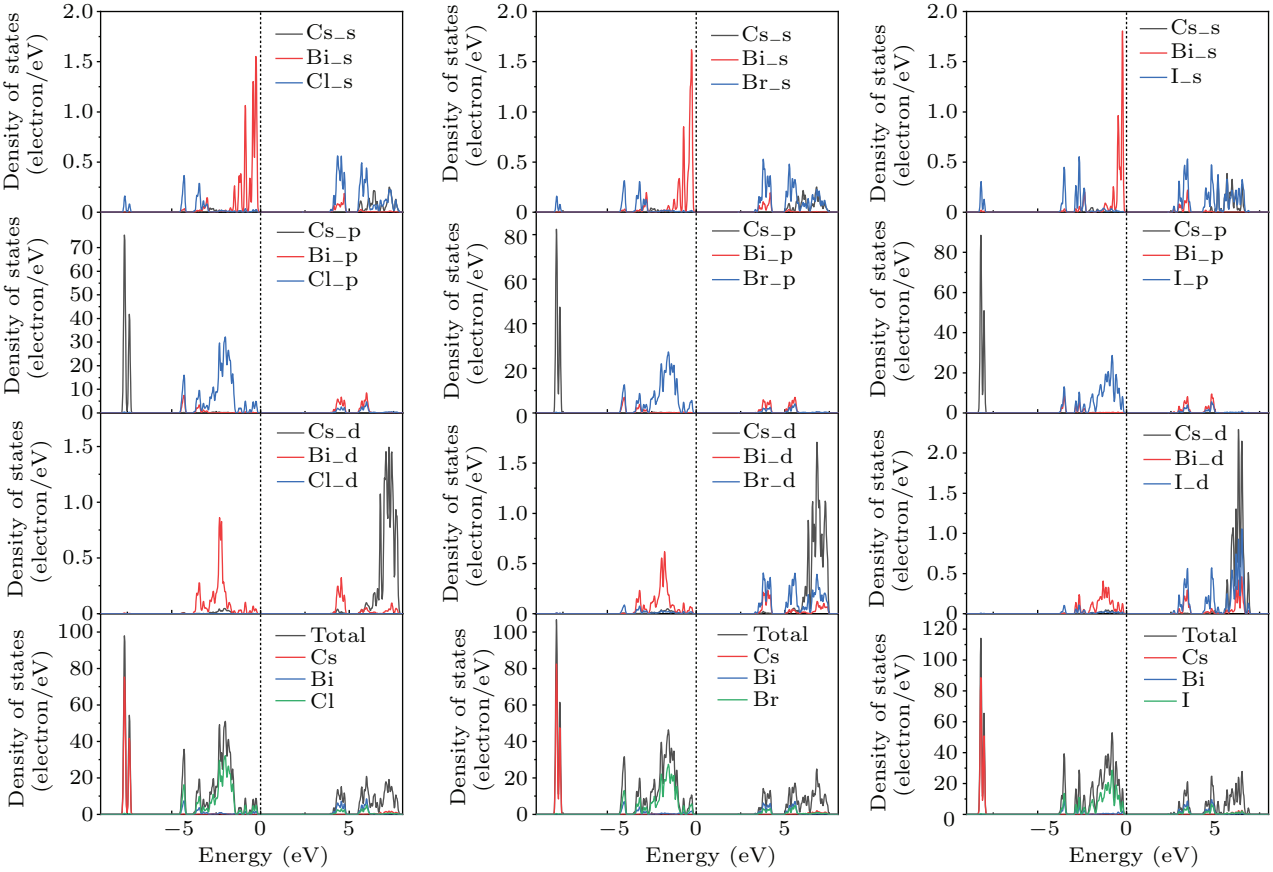


Fig. A2. The DOS of different orbitals and elements of monolayer $Cs_3Bi_2X_9$ (X = Cl, Br, I).

References

[1] Maughan A E, Ganose A M, Bordelon M M, Miller E M, Scanlon D O and Neilson J R 2016 *J. Am. Chem. Soc.* **138** 8453

[2] Ke W and Kanatzidis M G 2019 *Nat. Commun.* **10** 965

[3] Slavney A H, Hu T, Lindenberg A M and Karunadasa H I 2016 *J. Am. Chem. Soc.* **138** 2138

[4] Liu Y L, Yang C L, Wang M S, Ma X G and Yi Y G 2018 *J. Mater. Sci.* **54** 4732

[5] Luo J, Wang X, Li S, *et al.* 2018 *Nature* **563** 541

[6] Liu C, Wang Y, Geng H, Zhu T, Ertekin E, Gosztola D, Yang S, Huang J, Yang B, Han K, Canton S E, Kong Q, Zheng K and Zhang X 2019 *J. Am. Chem. Soc.* **141** 13074

[7] El Ajjouri Y, Chirvony V S, Vassilyeva N, Sessolo M, Palazon F and Bolink H J 2019 *J. Mater. Chem. C* **7** 6236

[8] Li H, Luo T, Zhang S, Sun Z, He X, Zhang W and Chang H 2020 *Energy Environ. Mater.* **4** 46

[9] Harikesh P C, Mulmudi H K, Ghosh B, Goh T W, Teng Y T, Thirumal K, Lockrey M, Weber K, Koh T M, Li S, Mhaisalkar S and Mathews N 2016 *Chem. Mater.* **28** 7496

[10] Mao L, Stoumpos C C and Kanatzidis M G 2019 *J. Am. Chem. Soc.* **141** 1171

[11] Cortecchia D, Dewi H A, Yin J, Bruno A, Chen S, Baikie T, Boix P P, Gr?tzel M, Mhaisalkar S, Soci C and Mathews N 2016 *Inorg. Chem.* **55** 1044

[12] Liu Q, Lin S Y, Mao W M, Chun L, Dan X, Ming D L and Gaoquan S 2018 *Nanoscale* **10** 6837

[13] Chen F, Zhen W H, Xi S Z, Zhi S H, Shuai W, Qi M J, Jun W, Mei L H and Hui L D 2019 *ACS Appl. Mater. Interfaces* **11** 8419

[14] Lanzetta L, Marin-Beloqui J M, Sanchez-Molina I, Ding D and Haque S A 2017 *ACS Energy Lett.* **2** 1662

[15] Pan L Y, Ding Y F, Yu Z L, Wan Q, Liu B and Cai M Q 2020 *J. Power Sources* **451** 227732

[16] Kim S Y, Yun Y, Shin S, Lee J H, Heo Y W and Lee S 2019 *Scr. Mater.* **166** 107

[17] Geng T, Wei S, Zhao W, Ma Z, Fu R, Xiao G and Zou B 2021 *Inorg. Chem. Front.* **8** 1410

[18] Liu Z L, Liu R R, Mu Y F, Feng Y X, Dong G X, Zhang M and Lu T B 2021 *Solar RRL* **5** 2000691

[19] Hu W, He X, Fang Z, Lian W, Shang Y, Li X, Zhou W, Zhang M, Chen T, Lu Y, Zhang L, Ding L and Yang S 2020 *Nano Energy* **68** 104362

[20] Sarkar A, Acharyya P, Sasmal R, Pal P, Agasti S S and Biswas K 2018 *Inorg. Chem.* **57** 15558

[21] D S M, D L P J, J P M, J P C, J H P, J C S and C P M 2002 *J. Phys.: Condens. Matter* **14** 2717

[22] Perdew J P, Burke K and Ernzerhof M 1996 *Phys. Rev. Lett.* **77** 3865

[23] Baroni S, Gironcoli S D and Corso A D 2001 *Rev. Mod. Phys.* **73** 515

[24] Le Bahers T, Rérat M and Sautet P 2014 *J. Phys. Chem. C* **118** 5997

[25] Grimme S, Antony J, Ehrlich S and Krieg H 2010 *J. Chem. Phys.* **132** 154104

[26] Kresse G and Furthmüller J 1996 *Phys. Rev. B* **54** 11169

[27] Yu B B, Liao M, Yang J X, Chen W, Zhu Y D, Zhang X S, Duan T, Yao W T, Wei S H and He Z B 2019 *J. Mater. Chem. A* **7** 8818

[28] Xiao Z W, Meng W W, Wang J B, Mitzi D B and Yan Y F 2017 *Mater. Horiz.* **4** 206

[29] Kudo A and Miseki Y 2009 *Chem. Soc. Rev.* **38** 253

[30] Palummo M, Bernardi M and Grossman J C 2015 *Nano Lett.* **15** 2794

[31] Wang Z, Altmann P, Gadermaier C, Yang Y, Li W, Ghirardini L, Trovatello C, Finazzi M, Duò L, Celebrano M, Long R, Akinwande D, Prezhdo O V, Cerullo G and Dal Conte S 2021 *Nano Lett.* **21** 2165

[32] Li P F and Wang Z W 2018 *J. Appl. Phys.* **123** 204308